Gang Lin[1], Samuel Chapman[1], Dmitry Garagash[2], Jérôme Fortin[1], and Alexandre Schubnel[1]

[1]Laboratoire de Géologie, UMR 8538, Ecole Normale Supérieure/CNRS, PSL Research University
[2]Department of Civil and Resource Engineering, Dalhousie University

April 12, 2024

Abstract

Understanding the coupling between rock permeability, pore pressure, and fluid flow is crucial, as fluids play an important role in the Earth's crustal dynamics. We measured the distribution of fluid pressure during fluid-flow experiments on two typical crustal lithologies, granite and basalt. Our results demonstrate that the pore-pressure distribution transitions from a linear to a non-linear profile as the imposed pore-pressure gradient is increased (from 2.5 MPa to 60 MPa) across the specimen. This non-linearity results from the effective pressure dependence of permeability, for which two analytical formulations were considered: an empirical exponential and a new micromechanics-based model. In both cases, the non-linearity of pore pressure distribution is well predicted. However, using a compilation of permeability vs. effective pressure data for granites and basalts, we show that our micromechanics-based model, which combines the rough crack asperity model and cubic law theories, outperforms the exponential formulation at low effective pressures.

Posted on 12 Apr 2024 — CC-BY 4.0 — https://doi.org/10.22541/essoar.171291920.01431352/v1 — This is a preprint and has not been peer-reviewed. Data may be preliminary.

Pressure dependence of permeability in cracked rocks: experimental evidence of non-linear pore-pressure gradients from local measurements

Gang Lin[1], Samuel Chapman[1], Dmitry Garagash[2], Jérôme Fortin[1] and Alexandre Schubnel[1]

1. Laboratoire de Géologie, Ecole Normale Supérieure/CNRS UMR 8538, PSL Research University, Paris, France.
2. Department of Civil and Resource Engineering, Dalhousie University, Halifax, Nova Scotia, Canada

Corresponding author: Gang Lin (gang@geologie.ens.fr)

Key points:

- Pore pressure was measured locally in rocks exhibiting pressure-dependent permeability.
- We observed a transition from linear to nonlinear pore pressure distribution with increasing fluid pressure gradients.
- A new, micromechanics-based, analytical model was developed for the pressure dependence of permeability in microcracked rocks.

Abstract:

Understanding the coupling between rock permeability, pore pressure, and fluid flow is crucial, as fluids play an important role in the Earth's crustal dynamics. We measured the distribution of fluid pressure during fluid-flow experiments on two typical crustal lithologies, granite and basalt. Our results demonstrate that the pore-pressure distribution transitions from a linear to a non-linear profile as the imposed pore-pressure gradient is increased (from 2.5 MPa to 60 MPa) across the specimen. This non-linearity results from the effective pressure dependence of permeability, for which two analytical formulations were considered: an empirical exponential and a new micromechanics-based model. In both cases, the non-linearity of pore pressure distribution is well predicted. However, using a compilation of permeability vs. effective pressure data for granites and basalts, we show that our micromechanics-based model, which combines the rough crack asperity model and cubic law theories, outperforms the exponential formulation at low effective pressures.

Plain Language Summary:

Fluids and fluid migrations play an important role in the Earth's crustal dynamics and how fluids migrate through a rock will depend primarily on permeability. However, the permeability of crustal rocks may exhibit important pressure dependence, because cracks and fractures will increasingly close with increasing tectonic pressure. In this experimental study, we show that the couplings between increasing pressure, crack closure, and permeability reduction may result in non-linear pore pressure distributions on a rock specimen at the laboratory scale, which confirms for the first time pioneering theoretical and experimental works. Two simple analytical expressions of the pressure dependence of permeability predict this non-linearity. One empirical expression, most commonly used in the literature, takes the form of an exponential. The second one, a new model, based on crack micromechanics, was developed within this work and shown to outperform the exponential formulation at low effective pressure.

1. Introduction

Fluid migration and pore pressure distribution in the crust are important parts of the Earth's system and have an impact on most geological activities, such as groundwater circulation (Corbet & Bethke, 1992; Thomas et al., 2023), mineral resources formation (Li et al., 2022; Tivey, 2007), magmatic fluid pressurizations (Fazio et al., 2017; Gueugneau et al., 2017; Manga & Brodsky, 2006), and induced earthquakes (Keranen et al., 2014; Kim et al., 2018). Indeed, recent tomographic studies on the Changning earthquake in China (Lei et al., 2019; Li et al., 2021) and the Pohang earthquake in South Korea (Kim et al. 2018; Yeo et al. 2020) have emphasized the crucial importance of pore pressure excess in triggering earthquakes (Ellsworth, 2013; Guglielmi et al., 2015). In the Earth's crust, the mechanisms that may lead to pore pressure excess involve complex couplings between stress (in the fluid and matrix), temperature, and rock physical properties (e.g. porosity and permeability) (Rice, 1992; Rice, 2006) or even, at greater depth, mineral dehydration (Brantut et al., 2010; Wong et al., 1997). However, in-situ measurements of pore pressure in the field are difficult outside of local measurements around boreholes.

It was generally considered during fluid injection into the subsurface that the front of micro-seismicity follows closely the pore pressure diffusion front (Shapiro & Dinske, 2009). In the last years, some publications have supported the view that the micro-seismicity front is more likely to be related to the propagation of a slow slip front, while the pore pressure diffusion front lags behind (Bhattacharya & Viesca, 2019; Danré et al., 2024; Eyre et al., 2019; Garagash et al., 2017; Guglielmi et al., 2015). To mitigate potential geological hazards associated with fluid pressure, a better understanding of the pore pressure diffusion and distribution laws in crystalline and/or low porosity/tight rocks is important.

The permeability of rocks has been studied experimentally for decades and was shown to exhibit important pressure dependence, mainly because of elastic crack-closure as (effective) confining pressure increases (Brace et al., 1968). Many empirical models were used to describe the permeability changes with effective stress, which can generally be divided into two classes of models: exponential or power law pressure dependence. David et al. (1994) used an exponential law to describe the permeability dependence of five kinds of sandstones. They also adopted such an exponential pressure dependence for the permeability of a natural Grimsel granodiorite (David et al., 2018), and finally concluded that this relationship was suitable for relatively high effective stress ranges. The exponential law model was also widely used in describing the pressure dependence of permeability in faults (Evans et al., 1997; Ji et al., 2023). A significant limitation of the exponential law model is its inability to provide accurate fits at a low effective pressure range. The power law is another method to characterize permeability pressure dependence (Ghabezloo et al., 2009; Morrow et al., 1984; Su et al., 2022). However, it cannot be regarded as a general constitutive relation due to its divergence at zero effective pressure (Jia et al., 2017; Zheng et al., 2015).

The pressure dependence of rock permeability has been used by David et al. (1994) and Rice (1992) to argue for the presence of non-linear pressure gradients across faults and within the crust. Another important question is the occurrence of non-linear pore pressure diffusion and distribution during laboratory experiments. While experimental inferences have been reported using strain gages (Garagash et al., 2017), new measurement techniques have recently been developed to measure the fluid pressure locally on samples in the laboratory. For instance, Dautriat et al. (2009) were able to measure the radial and axial permeability of cylindrical rock samples by injecting fluid and monitoring pore pressure along the sides of the specimens. Nicolas et al. (2020) monitored the diffusion of pore pressure pulses in intact andesite rock using fiber optic sensors and modeled this process by solving the diffusion equation. Brantut and Aben (2021) introduced newly developed strain-gauge based pore pressure transducers and used them on sandstone and granite. Proctor et al. (2020) pre-embedded sensors in a granite sample adjacent to a saw-cut plane to detect the variations in pore pressure during rupture nucleation and concluded that the effect of fluid pressure changes can exceed that of frictional variations. A similar experiment was conducted by Brantut (2020), who focused on fluid pressure drop induced by dilatancy and reported the occurrence of partial vaporization or degassing of fluid during rupture.

Here, we use a similar sensor design to that of Brantut and Aben (2021) to monitor the local pore pressure distribution in micro-cracked rocks under small (2.5 MPa) to large fluid pressure gradients (60 MPa). First, we measured the specimen's permeability as a function of effective pressure by applying a small pore pressure gradient (1 MPa). We then applied large pore pressure gradients and measured the pore pressure distribution along the length of the two samples. We discuss the observed variations of permeability and pore pressure distribution as a function of effective stress by comparing them to a new micromechanics-based model and an exponential model. Solving the diffusion equation for these two models, we compare our experimental measurements to theoretical predictions and compare our micromechanics-based model to an extensive set of experimental data found in the literature.

2. Experimental Methods

Here, compressive stress and compressive strain are positive, and confining pressure and pore pressure are denoted by Pc and p, respectively. The simple effective pressure is Pc-p and is denoted by P_{eff} (Terzaghi, 1925). The samples are crystalline rocks widely used in previous research (Brace et al., 1968; Fortin et al., 2011; Heap et al., 2018; Wang et al. 2013): Westerly granite and Etna basalt. Two cylindrical samples of 40 mm in diameter and 90 mm in length were prepared. The granite sample was heat-treated in three steps: i) the sample was heated up to 650 °C at a rate of 5 °C/min, ii) it was kept at the target temperature for 2 h, iii) then, the sample was left to cool down to ambient temperature. The initial porosity is 4.9% for the basalt and 3.7% for the heat-treated granite. Porosity was measured using the triple weight technique.

Experiments were performed using a hydraulic triaxial cell installed at the Laboratoire de Géologie of École Normale Supérieure in Paris (Borgomano et al., 2020). Two pumps (Quizix 6000-Series) were connected to the top and bottom of the sample to control the pore pressure. Confining and pore pressure were measured with an accuracy of approximately 10^{-2} MPa. Samples were jacketed with neoprene sleeves to isolate them from confining oil, and water was used as pore fluid. Internal pore pressure sensors were used to measure the pore pressure at different locations along the sample (Brantut & Aben, 2021). The accuracy of these internal pore pressure sensors is +/- 1 MPa. Details and calibration of these sensors are given in Text S1 of supporting information. In the case of the Westerly granite sample, 6 pore pressure sensors were installed along a double-line arrangement (Figure S1), and the measured pore pressure value is the average of that performed by 2 sensors at the same height. In the case of the basalt sample, 7 pore pressure sensors were used in a spiral arrangement (Figure 1a). Note that during this experiment, we will set the pore pressure measured by the first top sensor as the boundary pressure (see Figures 3a and 3b).

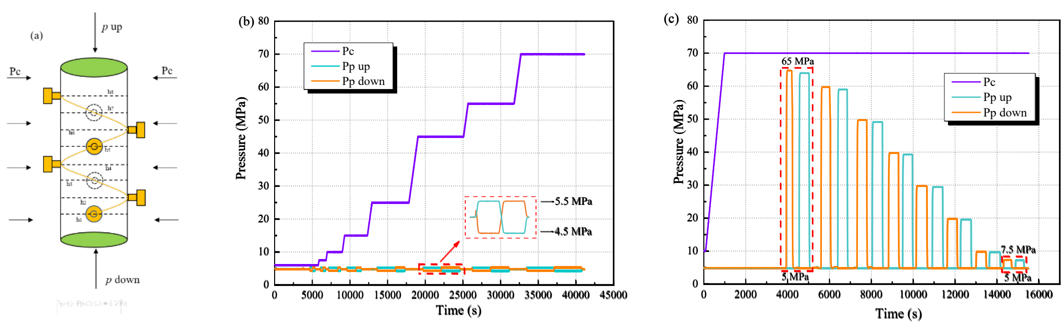

Figure 1. Experimental procedure. (a) Schematic diagram of a sample equipped with 8 internal pore pressure (p) sensors in a spiral arrangement (Etna basalt specimen). (b) Pressure loading path for permeability measurements with increasing confining pressures Pc, from 6 to 70 MPa, p being kept at 5 MPa. Permeability was measured using the constant flow method, with a pore pressure gradient kept at 1 MPa. (c) Pressure loading path for p distribution

measurements, for decreasing *p* gradients. *p* was measured locally using the internal *p* sensors, under constant confining pressure (70 MPa), and for *p* gradients ranging from 2.5 to 60 MPa.

As a first step, dry samples underwent two confining pressure cycles up to 70 MPa, to guarantee that the samples behaved purely elastically in the following steps. We then injected water into the samples until the pore pressure reached 5 MPa while maintaining a confining pressure of 10 MPa. Two experimental procedures were followed: i) classical permeability measurement under pressure (Figure 1b) and ii) pore pressure gradient experiment (Figure 1c). During the first procedure, permeability was measured using the steady-state method (e.g. Fortin et al. 2011; Ougier-Simonin et al., 2011) following the loading path in Figure 1b. At a given confining pressure, a 1 MPa pore pressure gradient was fixed (p = 5.5 MPa on one end and 4.5 MPa on the other end of the rock specimen), the fluid flow through the sample was measured, and permeability was inferred using Darcy's law. Permeability was measured twice at each effective pressure step by switching the flow direction, and a mean value was calculated.

In the second procedure, the pore pressure distribution was measured along the length of the sample under pore pressure gradients. First, the confining pressure was fixed to 70 MPa and the pore pressure to 5 MPa, as shown in Figure 1c. Then, the pore pressure on one end was increased to generate a pore pressure gradient along the sample's length. Pore pressure was measured locally, in the steady-state regime, by the internal pore pressure sensors. In total, 8 pore pressure gradients were investigated, starting from a large pore pressure gradient of 60 MPa (65 MPa on one side and 5 MPa on the other) to a small pore pressure gradient of 2.5 MPa (7.5 MPa on one side and 5 MPa on the other).

3. Experimental results

3.1 Pressure dependence of permeability

The permeability evolution of heat-treated Westerly granite and Etna basalt is shown in Figure 2a as a function of effective pressure. As reported by previous studies, the permeability of both rocks decreases with increasing effective pressure. Permeability of Etna Basalt decreases almost 20-fold, from about 3×10^{-17} m² at an effective pressure of 1 MPa to about 2×10^{-18} m² at 65 MPa. The permeability of Westerly granite exhibits an even greater pressure dependence, from about 6×10^{-18} m² to 2×10^{-19} m² within the same differential pressure range. Most of the decrease in permeability (80% for Etna Basalt and 90% for Westerly granite) occurs before 20 MPa effective pressure.

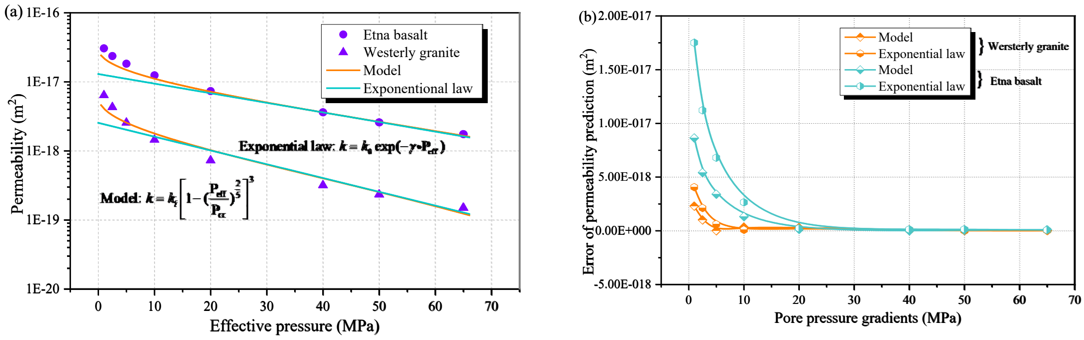

Figure 2. Permeability evolution and error analyses in heat-treated Westerly granite and Etna basalt. (a) Permeability evolution: the experimental data for permeability of heat-treated Westerly granite and Etna basalt are expressed by triangles and circles, respectively. Orange and blue solid lines are best fits using the new micromechanics-based model model and exponential law respectively. (b) Error analyses: Orange and blue solid lines are differential permeability between experimental data and theoretical predictions for heat-treated Westerly granite and Etna basalt. The points of hexagonal and quadrilateral correspond to the prediction error expressed using the exponential law and the new micromechanics-based model, respectively. Note that both figures reflect that the new micromechanics-based model and exponential law models converge at high effective pressure, but that the new micromechanics-based model gives better prediction at low effective pressure.

3.2 Pore pressure distribution under large pore-pressure gradient

Using the local pore pressure sensors, the distribution of pore pressure could be monitored both in Westerly granite and Etna basalt, under low to high pore pressure gradients for gradients across the specimen ranging from 2.5 to 60 MPa (Figure 3). As expected from Darcy's law for a constant (pressure independent) permeability, pore pressure varies linearly as a function of sample length for low to moderate pore-pressure gradients (2.5, 5, and 15 MPa). However, as the pore pressure gradient is increased (from 25 MPa and above and up to 60 MPa), the distribution of pore pressure becomes non-linear within the rock specimen. The same phenomenon was observed for both rocks (see Figure 3a and 3b) and is therefore not affected by the magnitude of permeability, but rather by its pressure dependence, i.e. the permeability not being constant along the sample's length. Interestingly, one should note that this corresponds to a situation of pore-pressure excess when compared to what would be a linear distribution of pore pressure, i.e. pore pressure is higher than what it would be for linear-gradient (and a constant permeability).

Excess in pore pressure increases with increasing gradients, and at the highest gradients, the pore pressure remains close to that of the high-end pore pressure for close to 50% of the sample's length. This effect is more pronounced in Westerly granite than in Etna basalt, which results from the difference in the pressure dependence of permeability of both rocks. To be clearer, the more pronounced the pressure sensitivity, the more pronounced the pore pressure excess and the more abrupt (spatially) the pore pressure shutdown at the low (pore pressure) end of the specimen.

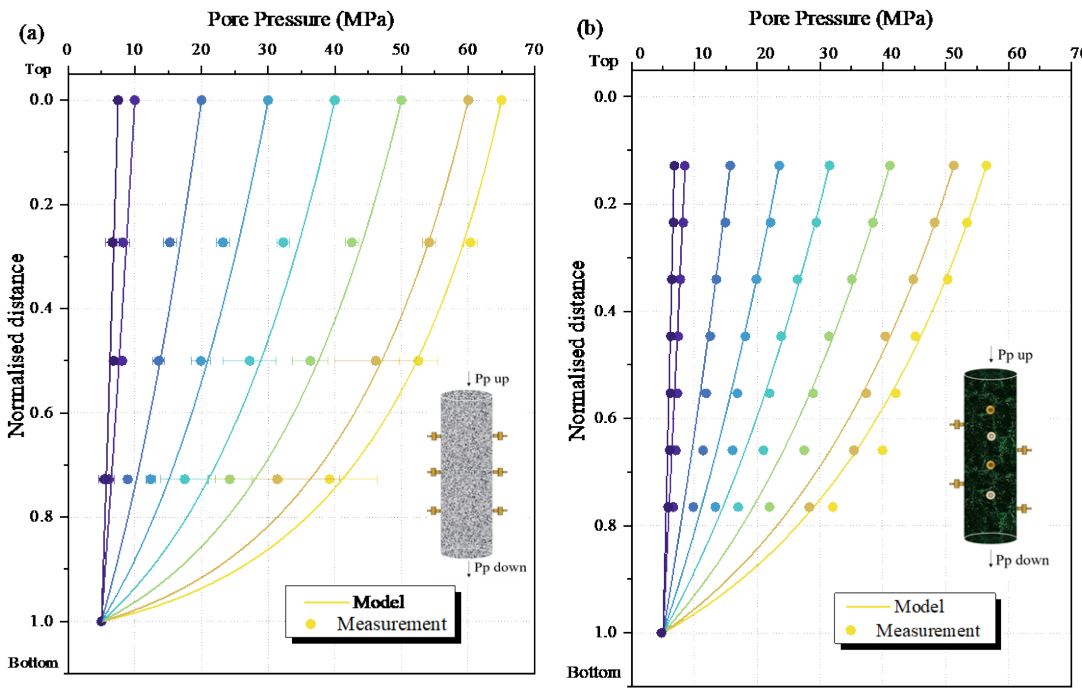

Figure 3. Pore pressure (p) distribution as a function of sample length under varying p gradients of (a) heat-treated Westerly granite and (b) Etna basalt. Low p gradients correspond to cold (blue) colors; large gradients to warm (yellow) colors; circles correspond to local p measurements performed by the internal p sensors; solid lines to theoretical predictions using the new micromechanics-based model (equations 1 and 3) for p distribution.

4. Discussion

4.1 Pore pressure distribution with pressure dependent permeability

In our experiments, the pore pressure p was only measured at the steady state. Hence the pore pressure distribution should follow the diffusion equation under the steady state:

$$\frac{d}{dz}\left[-\frac{k}{\eta}\frac{dp}{dz}\right] = 0 \qquad (1)$$

where k is permeability; η is the fluid viscosity. The pressure distribution, i.e. the relationship between pore pressure p and the location along the z-axis in equation (1) will therefore depend on the functional form of the pressure dependence of permeability k. Following our measurements, two functional forms may be used to express the permeability effective pressure dependence: an exponential form or a micromechanics-based model.

The exponential law is generally expressed as (David et al., 1994):

$$k = k_0 \, e^{-\gamma (P_{eff})} \qquad (2)$$

where k_0 is the initial permeability at zero pressure; γ is a coefficient called stress sensitivity factor (1/Pa), inherent to the rock sample. The micromechanics-based model used in this study is:

$$k = k_o \left[1 - \left(\frac{P_{eff}}{P_{cc}}\right)^{\frac{2}{5}}\right]^3 \qquad (3)$$

with $P_{eff} \leq P_{cc}$ and where k_0 is the initial permeability at zero pressure and P_{cc} is the crack closing pressure, an inherent parameter of the rock sample and characteristic pressure above which all the cracks in the specimen can be considered as closed. P_{cc} is therefore related to the consolidation stress (maximum previously experienced pressure) of rock. Details on the derivation are presented in Text S2 of the supporting information. One should note here that: i) although empirical, this new model is physics-based, as the exponent 2/5 arises from rough crack asperity model (Brown & Scholz, 1985; Gavrilenko & Gueguen, 1989; Johnson, 1982; Walsh, 1981), while the exponent 3 arises from the well-established cubic-law for permeability (Zimmerman & Bodvarsson, 1996); ii) it replaces the complex microstructure of a cracked rock by that of an idealized single rough crack, with a roughness distribution equiprobable at all heights below that of the initial aperture. Such an asperity distribution was proven to best fit experimental permeability data (Gavrilenko & Gueguen, 1989). In essence, the law describes the permeability evolution (cubic law) of a rough crack under external pressure/normal stress.

As shown in Figure 2a, the evolution of permeability k with effective stress P_{eff} for both samples, is well described by the exponential law and the micromechanics-based model. Fitting parameters (k_0, γ, and P_{cc}) are given in Table S1 of supporting information. k_0 values obtained for the exponential law are lower than those obtained for the micromechanics-based model which can readily be explained by the fact the micromechanics-based model provides a better fitting at low effective pressure, in a range of pressure where the exponential law underestimates the permeability. Not surprisingly, the inverse pressure sensitivity parameter $1/\gamma$ of the exponential law is approximately one order of magnitude lower than the crack closure pressure P_{cc} of our micromechanics-based model. Nevertheless, both formulations converge at high effective pressure. Figure 2b quantifies the fitting of the error of both laws. As seen in Figure 2b, our micromechanics-based model captures the evolution of permeability under low effective pressure conditions better. Importantly the micromechanics-based model does not have the low-pressure limitations of the exponential law. However, distinguishing the fitting effects becomes challenging when the effective pressure exceeds 20 MPa.

Substituting the exponential law (equation 2) into the diffusion equation (equation 1), we get the following solution (modified from Rice 1992 or David et al. 1994):

$$p(z) = \frac{\ln}{\alpha}\left[\left(e^{\gamma P_{\text{down}}} - e^{\gamma P_{\text{up}}}\right)\frac{z}{L} + e^{\gamma P_{\text{up}}}\right] \qquad (4)$$

where P_{down} and P_{up} are the pore pressure boundary conditions set at the top and bottom of the specimen. From equation (4), the pore pressure p can be predicted at any position z by determining the stress sensitivity factor γ with given boundary conditions. As presented in Table S1 of the supporting information, the stress sensitivity factors γ for Westerly granite and Etna Basalt are 0.046 and 0.032 respectively, and the solutions for pore pressure distribution in our specimen are shown as solid lines in Figures S2a and S2b. These theoretically predicted trends are indeed consistent with those of the experimental data points (Figure S2).

Similarly, another solution can be obtained by substituting the micromechanics-based model (equation 3) into the diffusion equation (equation 1):

$$p^*(1 - \tfrac{15}{7}p^{*\frac{2}{5}} + \tfrac{5}{3}p^{*\frac{4}{5}} - \tfrac{5}{11}p^{*\frac{6}{5}}) = Cz - D \qquad (5)$$

Here $p^* = \frac{Peff}{P_{cc}}$, and C and D are constants which detailed expressions are given in Text S3 of supporting information. The functional form of equation (5) is interesting, as a linear pore pressure gradient is readily retrieved at small p^* (i.e. disregarding the 1st, 2nd, and 3rd order terms in $p^{*2/5}$). Equation (5) can thus be interpreted as a Taylor series expansion in $p^{*2/5}$ with respect to the reference linear case. The analytical solution of $p^*(z)$ is non-trivial because of the polynomial nature of equation (5). But a solution can be retrieved by looking for the pore pressure value p (ranging between P_{down} and P_{up}) that minimizes the difference between the left hand-side and right hand-side of equation (5) at a given position z. These best-fit solutions are shown as solid lines in Figures 3a and 3b, which shows that equation (5) indeed predicts the trend observed in experimental data. In particular, our micromechanics-based model predicts a transition from linear to non-linear pore pressure gradients when increasing pore pressure difference is imposed at the two ends of the rock specimen.

We also compared the error in the prediction of the measured pore pressure profile with theoretical solutions using the exponential law and the micromechanics-based model (Figure S3). The error in predicting the pore pressure profiles using the exponential law and the micromechanics-based model is almost the same, especially for low pore pressure gradients, which also correspond to relatively high effective pressure, where the permeability predictions are equivalent. Again, the predictive performance of the micromechanics-based model slightly surpasses that of the exponential law as the pore pressure gradients increase. This is particularly true when the pore pressure gradient reaches 60 MPa, for which errors in predictions obtained with the micromechanics-based model for Westerly granite and Etna Basalt are 2.7% and 5.4%, respectively, in contrast to 3.3% and 6.0% for the predictions based on the exponential law.

This highlights once again the capacity of the micromechanics-based model to better capture permeability and pore evolutions at low effective pressure.

Finally, note that only the Terzaghi effective pressure was used, i.e. $Peff$ = Pc - p, while previous studies have demonstrated that the effective pressure coefficient (Biot coefficient for pressure) was close to, but generally lower than 1 in crystalline rocks (Bernabe. 1986, 1987, 1988). It is foreseeable that our predictions might have been better if an effective pressure coefficient slightly lower than one had been measured and considered. In any case, the large errors observed in Figure S3 are probably due to limitations of our sensor sensitivity, which remains the limiting factor.

4.2 Pressure dependence of permeability for crystalline rocks

The evolution of permeability of porous and cracked rocks with effective pressure has been extensively studied (e.g. Bernabe, 1986; Brace et al., 1968; David et al., 1994; Dong et al., 2010; Heller et al., 2014; Davies & Davies, 2001; Gray & Fatt, 1963). In general, either the exponential law $k = k_0\, \mathrm{e}^{-\gamma\,(\mathrm{P_{eff}})}$ or a power-law of the form $k = k_0\, (\mathrm{P_{eff}})^{-\mathrm{m}}$ have been employed to describe the pressure dependence of permeability. However, neither the exponential law nor the power-law, have a clear micromechanical background to support their formalism, and should be considered empirical mathematical approximations. In addition, such power-law formalism for the permeability pressure dependence presents three important caveats: i) a dimensional problem, which one can circumvent by normalization; ii) the arbitrary nature of the exponent *m,* which needs to be fitted on a case-by-case basis; iii) the asymptotic convergence to zero when the effective pressure gets close to zero (Su et al., 2022; Zheng et al., 2015). We showed above that the exponential law is indeed efficient in predicting both the permeability and pore pressure evolution at high effective pressure. However, problems arise at low effective pressures.

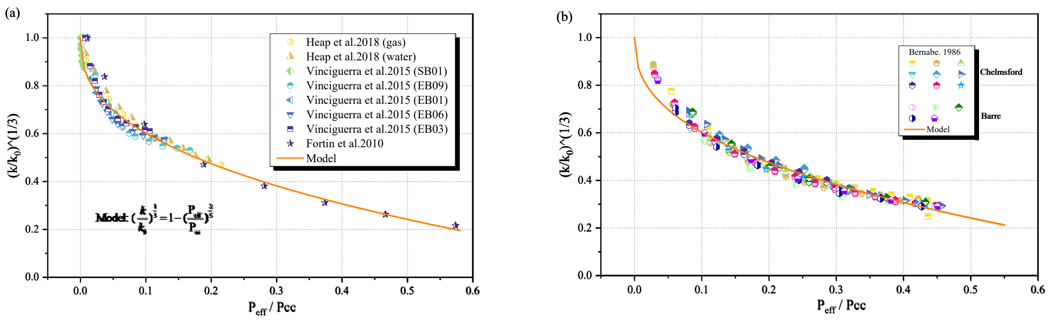

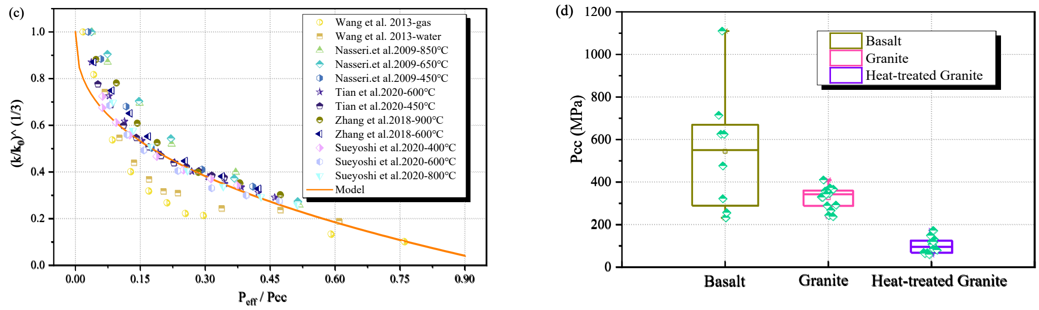

Figure 4. Validation of the new micromechanics-based model. Comparison of published experimental data and the new micromechanics-based model for (a) basalts, (b) natural granites and (c) heated treated granites. The data have been normalized according to the format of the new micromechanics-based model. The orange line is the normalized model ($(\frac{k}{k_o})^{\frac{1}{3}}$=1-$(\frac{Peff}{Pcc})^{\frac{2}{5}}$). (d) The ranges of closure pressure *Pcc* for basalt (green), granite (pink), and heat-treated granite (blue), with medium *Pcc* being 551, 343, and 96 MPa, respectively.

Figure 4 displays a large compilation of experimental data on the permeability evolution with effective pressure in crystalline rocks. Three cases were considered: granites, basalts, and heat-treated granites, respectively displayed in Figures 4a, 4b, and 4c. For each data set, a best fit was performed using our micromechanics-based model. One can see that when plotting $(k/ko)^{1/3}$ as a function of the normalized effective pressure (*Peff/Pcc*), the pressure dependence of permeability of all rock types converges with the micromechanics-based model prediction. This is particularly true for basalts and natural granites (Figures 4a and 4b). Note here that the Chelmsford and Barre granites data were cored from three different directions and showed relative homogenous permeability (Bernabe, 1986). However, the predictive performance of our model on heat-treated granites was not as strong as that observed in natural basalts and granites, and the data exhibited increased dispersion along the trendline in this case (see Figure 4c). We suspect that differences in the heat-treatment procedures impact the homogeneity of these data sets, which, in turn, affects the model's predictions for experimental data. Finally, an additional output of these fits is the crack closure pressures *Pcc* obtained for each of these data sets. One can see that *Pcc* obtained for natural granites is close to a median value of 340 +/- 3 MPa. This is a satisfying result, as larger dispersion was observed by David et al. (1994) for the pressure sensitivity parameter $1/\gamma$ of granite using the exponential law, probably because, when using the exponential law, the best-fit parameter will largely depend on the pressure range of fitting, as we have seen how the exponential fails at predicting the low effective pressure permeability evolution. The *Pcc* obtained for basalts is much more dispersed (550 +/- 1 MPa), which probably arises from the inherent variety of basalt permeability, depending on their cooling conditions when they were emplaced. Basalt, in the rock mechanics community, also refers to the large variety of rocks, sometimes a bit more acidic than basalt per se for the petrology/volcanology community (Heap et al., 2018). The P_{cc} for heat-treated granites is smaller, centered around 95 +/- 1 MPa, but quite dispersed, again probably due to the variety in heat-treatment processes in these studies.

Finally, it is important to stress that an important limitation of our micromechanics-based model is that the predicted permeability k becomes negative when effective stress P_{eff} exceeds that of the closing pressure P_{cc}. A similar phenomenon is also observed in Walsh's model (equation A-4). However, this cannot occur, as when the applied effective pressure increases, an increasing number of cracks will close, which will require an even higher pressure to fully seal the remaining cracks. P_{cc} is therefore related to the maximum pressure previously experienced by a rock, or the maximum consolidation stress, in such a way that previous experimental loadings or burial depth will contribute to the P_{cc}. In other words, P_{cc} should increase with increasing applied P_{eff}. For the P_{cc} determined above for natural granites and basalts, the situation ($P_{eff}/P_{cc} > 1$) cannot occur within the first 10-20km of the brittle crust, and perhaps even below, as elevated (up to lithostatic) pore pressures are thought to be prevalent at greater depths (David et al., 1994; Miller et al., 2004). At such depth, the Terzaghi effective pressure approximation probably also reaches its limit of applicability, as the Biot coefficient for effective pressure is expected to fall close to zero somewhere within the ductile/plastic regime (Hirth & Beeler, 2015).

5. Conclusion

Non-linear pore pressure distribution arises due to non-linear changes in permeability k in response to a significant pore-pressure gradient. Our experiments involving different pore pressure gradient measurements indeed show that the pore pressure distribution in crystalline/cracked rocks transitions from linear under low pore-pressure gradients to non-linear under high pore-pressure gradients, which results from the pressure dependence of permeability.

The pore pressure distribution at elevated pressure gradients can be predicted by solving the diffusion equation, which is achieved by describing the pressure dependence of permeability using either an empirical exponential law or a new micromechanics-based model. This new model, derived from a micromechanical analysis, is based on a combination of i) the aperture evolution of a rough crack under applied stress; ii) the cubic law, a well-established law to describe laminar flow within single fractures (Zimmerman & Bodvarsson, 1996). One should stress here that this new formalism results from an important simplification of previous analysis performed by Gavrilenko and Gueguen (1989) and has the potential to predict the generation and maintenance of pore pressure in crystalline rocks, over the entire range of effective pressures expected within the brittle crust.

Acknowledgments

There are no conflicts of interest among the authors. The first author acknowledges China Scholarship Council for providing funding to perform this study at ENS. This work was supported by the European Research Council Grant 681346 REALISM and the Centre National de la Recherche Scientifique via the program "Tellus-Aleas" of the Institut National des Sciences de l'Univers.

Data Availability Statement

The experimental data from the present study are available in Figshare, (https://doi.org/10.6084/m9.figshare.25315504).

References

Bernabe, Y. (1986). The effective pressure law for permeability in Chelmsford granite and Barre granite. *International Journal of Rock Mechanics and Mining Sciences & Geomechanics Abstracts*, *23*(3), 267–275. https://doi.org/10.1016/0148-9062(86)90972-1

Bernabe, Y. (1987). The effective pressure law for permeability during pore pressure and confining pressure cycling of several crystalline rocks. *Journal of Geophysical Research: Solid Earth*, *92*(B1), 649–657. https://doi.org/10.1029/JB092iB01p00649

Bernabe, Y. (1988). Comparison of the effective pressure law for permeability and resistivity formation factor in Chelmsford granite. *Pure and Applied Geophysics*, *127*, 607–625. https://doi.org/10.1007/BF00881747

Brantut, N., Schubnel, A., Corvisier, J., & Sarout, J. (2010). Thermochemical pressurization of faults during coseismic slip. *Journal of Geophysical Research: Solid Earth*, *115*(B5), 2009JB006533. https://doi.org/10.1029/2009JB006533

Brantut, N. (2020). Dilatancy-induced fluid pressure drop during dynamic rupture: Direct experimental evidence and consequences for earthquake dynamics. *Earth and Planetary Science Letters*, *538*, 116179. https://doi.org/10.1016/j.epsl.2020.116179

Brantut, N., & Aben, F. M. (2021). Fluid pressure heterogeneity during fluid flow in rocks: new laboratory measurement device and method. *Geophysical Journal International*, *225*(2), 968–983. https://doi.org/10.1093/gji/ggab019

Brace, W. F., Walsh, J. B., & Frangos, W. T. (1968). Permeability of granite under high pressure. *Journal of Geophysical Research*, *73*(6), 2225–2236. https://doi.org/10.1029/JB073i006p02225

Brown, S. R., & Scholz, C. H. (1985). Closure of random elastic surfaces in contact. *Journal of Geophysical Research: Solid Earth*, *90*(B7), 5531–5545. https://doi.org/10.1029/JB090iB07p05531

Bhattacharya, P., & Viesca, R. C. (2019). Fluid-induced aseismic fault slip outpaces pore-fluid migration. *Science*, *364*(6439), 464–468. https://doi.org/10.1126/science.aaw7354

Borgomano, J. V. M., Gallagher, A., Sun, C., & Fortin, J. (2020). An apparatus to measure elastic dispersion and attenuation using hydrostatic- and axial-stress oscillations under undrained conditions. *Review of Scientific Instruments*, *91*(3), 034502. https://doi.org/10.1063/1.5136329

Corbet, T. F., & Bethke, C. M. (1992). Disequilibrium fluid pressures and groundwater flow in the western Canada sedimentary basin. *Journal of Geophysical Research: Solid Earth*, *97*(B5), 7203–7217. https://doi.org/10.1029/91JB02993

David, C., Wassermann, J., Amann, F., Lockner, D. A., Rutter, E. H., Vanorio, T., et al. (2018). KG^2B, a collaborative benchmarking exercise for estimating the permeability of the Grimsel granodiorite – Part 1: measurements, pressure dependence and pore-fluid effects. *Geophysical Journal International*, *215*(2), 799–824. https://doi.org/10.1093/gji/ggy304

David, C., Wong, T.-F., Zhu, W., & Zhang, J. (1994). Laboratory measurement of compaction-induced permeability change in porous rocks: Implications for the generation and maintenance of pore pressure excess in the crust. *Pure and Applied Geophysics*, *143*(1–3), 425–456. https://doi.org/10.1007/BF00874337

Danré, P., Garagash, D., De Barros, L., Cappa, F., & Ampuero, J. (2024). Control of Seismicity Migration in Earthquake Swarms by Injected Fluid Volume and Aseismic Crack Propagation. *Journal of Geophysical Research: Solid Earth*, *129*(1), e2023JB027276. https://doi.org/10.1029/2023JB027276

Dautriat, J., Gland, N., Guelard, J., Dimanov, A., & Raphanel, J. L. (2009). Axial and radial permeability evolutions of compressed sandstones: end effects and shear-band induced permeability anisotropy. *Pure and Applied Geophysics*, *166*, 1037–1061. https://doi.org/10.1007/s00024-009-0495-0

Dong, J.-J., Hsu, J.-Y., Wu, W.-J., Shimamoto, T., Hung, J.-H., Yeh, E.-C., et al. (2010). Stress-dependence of the permeability and porosity of sandstone and shale from TCDP Hole-A. *International Journal of Rock Mechanics and Mining Sciences*, *47*(7), 1141–1157. https://doi.org/10.1016/j.ijrmms.2010.06.019

Ellsworth, W. L. (2013). Injection-Induced Earthquakes. *Science*, *341*(6142), 1225942. https://doi.org/10.1126/science.1225942

Evans, J. P., Forster, C. B., & Goddard, J. V. (1997). Permeability of fault-related rocks, and implications for hydraulic structure of fault zones. *Journal of Structural Geology*, *19*(11), 1393–1404. https://doi.org/10.1016/S0191-8141(97)00057-6

Eyre, T. S., Eaton, D. W., Garagash, D. I., Zecevic, M., Venieri, M., Weir, R., & Lawton, D. C. (2019). The role of aseismic slip in hydraulic fracturing–induced seismicity. *Science Advances*, *5*(8), eaav7172. https://doi.org/10.1126/sciadv.aav7172

Fazio, M., Benson, P. M., & Vinciguerra, S. (2017). On the generation mechanisms of fluid-driven seismic signals related to volcano-tectonics. *Geophysical Research Letters*, *44*(2), 734–742. https://doi.org/10.1002/2016GL070919

Fortin, J., Stanchits, S., Vinciguerra, S., & Guéguen, Y. (2011). Influence of thermal and mechanical cracks on permeability and elastic wave velocities in a basalt from Mt. Etna volcano subjected to elevated pressure. *Tectonophysics*, *503*(1–2), 60–74.

Garagash, D., Brantut, N., Schubnel, A., & Bhat, H. S. (2017). Generation and maintenance of low effective pressures due to fluid flow in fractured rocks. In *AGU Fall Meeting Abstracts* (Vol. 2017, pp. S43B-0859). Retrieved from https://ui.adsabs.harvard.edu/abs/2017AGUFM.S43B0859G/abstract

Gavrilenko, P., & Gueguen, Y. (1989). Pressure dependence of permeability: a model for cracked rocks. *Geophysical Journal International*, *98*(1), 159–172. https://doi.org/10.1111/j.1365-246X.1989.tb05521.x

Ghabezloo, S., Sulem, J., Guédon, S., & Martineau, F. (2009). Effective stress law for the permeability of a limestone. *International Journal of Rock Mechanics and Mining Sciences*, *46*(2), 297–306. https://doi.org/10.1016/j.ijrmms.2008.05.006

Gray, D. H., & Fatt, I. (1963). The effect of stress on permeability of sandstone cores. *Society of Petroleum Engineers Journal*, *3*(02), 95–100. https://doi.org/10.2118/531-PA

Gueugneau, V., Kelfoun, K., Roche, O., & Chupin, L. (2017). Effects of pore pressure in pyroclastic flows: Numerical simulation and experimental validation. *Geophysical Research Letters*, *44*(5), 2194–2202. https://doi.org/10.1002/2017GL072591

Guglielmi, Y., Cappa, F., Avouac, J.-P., Henry, P., & Elsworth, D. (2015). Seismicity triggered by fluid injection–induced aseismic slip. *Science*, *348*(6240), 1224–1226. https://doi.org/10.1126/science.aab0476

Heller, R., Vermylen, J., & Zoback, M. (2014). Experimental investigation of matrix permeability of gas shales. *AAPG Bulletin*, *98*(5), 975–995. https://doi.org/10.1306/09231313023

Hirth, G., & Beeler, N. M. (2015). The role of fluid pressure on frictional behavior at the base of the seismogenic zone. *Geology*, *43*(3), 223–226. https://doi.org/10.1130/G36361.1

Keranen, K. M., Weingarten, M., Abers, G. A., Bekins, B. A., & Ge, S. (2014). Sharp increase in central Oklahoma seismicity since 2008 induced by massive wastewater injection. *Science*, *345*(6195), 448–451. https://doi.org/10.1126/science.1255802

Ji, Y., Zhang, W., Hofmann, H., Chen, Y., Kluge, C., Zang, A., & Zimmermann, G. (2023). Modelling of fluid pressure migration in a pressure sensitive fault zone subject to cyclic injection and implications for injection-induced seismicity. *Geophysical Journal International*, *232*(3), 1655–1667. Retrieved from https://academic.oup.com/gji/article-abstract/232/3/1655/6767592

Jia, C., Xu, W., Wang, H., Wang, R., Yu, J., & Yan, L. (2017). Stress dependent permeability and porosity of low-permeability rock. *Journal of Central South University*, *24*(10), 2396–2405. https://doi.org/10.1007/s11771-017-3651-1

Johnson, K. L. (1982). One Hundred Years of Hertz Contact. *Proceedings of the Institution of Mechanical Engineers*, *196*(1), 363–378. https://doi.org/10.1243/PIME_PROC_1982_196_039_02

Kim, K.-H., Ree, J.-H., Kim, Y., Kim, S., Kang, S. Y., & Seo, W. (2018). Assessing whether the 2017 M_w 5.4 Pohang earthquake in South Korea was an induced event. *Science*, *360*(6392), 1007–1009. https://doi.org/10.1126/science.aat6081

Lei, X., Wang, Z., & Su, J. (2019). The December 2018 ML 5.7 and January 2019 ML 5.3 earthquakes in South Sichuan basin induced by shale gas hydraulic fracturing. *Seismological Research Letters*, *90*(3), 1099–1110. https://doi.org/10.1785/0220190029

Li, T., Sun, J., Bao, Y., Zhan, Y., Shen, Z.-K., Xu, X., & Lasserre, C. (2021). The 2019 Mw 5.8 Changning, China earthquake: A cascade rupture of fold-accommodation faults induced by fluid injection. *Tectonophysics*, *801*, 228721. https://doi.org/10.1016/j.tecto.2021.228721

Li, X., Chen, S., Wang, Y., Zhang, Y., Wang, Y., Wu, J., et al. (2022). Influence of Pore Structure Particularity and Pore Water on the Occurrence of Deep Shale Gas: Wufeng–Longmaxi Formation, Luzhou Block, Sichuan Basin. *Natural Resources Research*, *31*(3), 1403–1423. https://doi.org/10.1007/s11053-022-10041-y

Manga, M., & Brodsky, E. (2006). Seismic triggering of eruptions in the far field: Volcanoes and geysers. *Annual Review of Earth and Planetary Sciences*, 34(1), 263–291. https://doi.org/10.1146/annurev.earth.34.031405.125125

Miller, S. A., Collettini, C., Chiaraluce, L., Cocco, M., Barchi, M., & Kaus, B. J. (2004). Aftershocks driven by a high-pressure CO2 source at depth. *Nature*, *427*(6976), 724–727. https://doi.org/10.1038/nature02251

Morrow, C. A., Shi, L. Q., & Byerlee, J. D. (1984). Permeability of fault gouge under confining pressure and shear stress. *Journal of Geophysical Research: Solid Earth*, *89*(B5), 3193–3200. https://doi.org/10.1029/JB089iB05p03193

Nicolas, A., Blöcher, G., Kluge, C., Li, Z., Hofmann, H., Pei, L., et al. (2020). Pore pressure pulse migration in microcracked andesite recorded with fibre optic sensors. *Geomechanics for Energy and the Environment*, *24*, 100183. https://doi.org/10.1016/j.gete.2020.100183

Ougier-Simonin, A., Guéguen, Y., Fortin, J., Schubnel, A., & Bouyer, F. (2011). Permeability and elastic properties of cracked glass under pressure. *Journal of Geophysical Research*, *116*(B7), B07203. https://doi.org/10.1029/2010JB008077

Proctor, B., Lockner, D. A., Kilgore, B. D., Mitchell, T. M., & Beeler, N. M. (2020). Direct Evidence for Fluid Pressure, Dilatancy, and Compaction Affecting Slip in Isolated Faults. *Geophysical Research Letters*, *47*(16), e2019GL086767. https://doi.org/10.1029/2019GL086767

Rice, J. R. (1992). Fault stress states, pore pressure distributions, and the weakness of the San Andreas fault. In *International geophysics* (Vol. 51, pp. 475–503). Elsevier. Retrieved from https://www.sciencedirect.com/science/article/pii/S0074614208628351

Rice, J. R. (2006). Heating and weakening of faults during earthquake slip. *Journal of Geophysical Research: Solid Earth*, *111*(B5), 2005JB004006. https://doi.org/10.1029/2005JB004006

Shapiro, S. A., & Dinske, C. (2009). Fluid-induced seismicity: Pressure diffusion and hydraulic fracturing. *Geophysical Prospecting*, *57*(2), 301–310. https://doi.org/10.1111/j.1365-2478.2008.00770.x

Su, T., Zhou, H., Zhao, J., Liu, Z., & Deng, H. (2022). A modeling approach to stress-dependent porosity and permeability decays of rocks. *Journal of Natural Gas Science and Engineering*, *106*, 104765. https://doi.org/10.1016/j.jngse.2022.104765

Terzaghi, K. (1925). *Erdbaumechanik auf bodenphysikalischer Grundlage*. F. Deuticke.

Thomas, A., Fortin, J., Vittecoq, B., & Violette, S. (2023). Earthquakes and Heavy Rainfall Influence on Aquifer Properties: A New Coupled Earth and Barometric Tidal Response Model in a Confined Bi-Layer Aquifer. *Water Resources Research*, *59*(4), e2022WR033367. https://doi.org/10.1029/2022WR033367

Tivey, M. K. (2007). Generation of seafloor hydrothermal vent fluids and associated mineral deposits. *Oceanography*, *20*(1), 50–65. https://www.jstor.org/stable/24859975

Wang, X., Schubnel, A., Fortin, J., Guéguen, Y., & Ge, H. (2013). Physical properties and brittle strength of thermally cracked granite under confinement. *Journal of Geophysical Research: Solid Earth*, *118*(12), 6099–6112. https://doi.org/10.1002/2013JB010340

Wong, T., Ko, S., & Olgaard, D. L. (1997). Generation and maintenance of pore pressure excess in a dehydrating system 2. Theoretical analysis. *Journal of Geophysical Research: Solid Earth*, *102*(B1), 841–852. https://doi.org/10.1029/96JB02484

Yeo, I. W., Brown, M. R. M., Ge, S., & Lee, K. K. (2020). Causal mechanism of injection-induced earthquakes through the Mw 5.5 Pohang earthquake case study. *Nature Communications*, *11*(1), 2614. Retrieved from https://www.nature.com/articles/s41467-020-16408-0

Zheng, J., Zheng, L., Liu, H.-H., & Ju, Y. (2015). Relationships between permeability, porosity and effective stress for low-permeability sedimentary rock. *International Journal of Rock Mechanics and Mining Sciences*, *78*, 304–318. https://doi.org/10.1016/j.ijrmms.2015.04.025

Zimmerman, R. W., & Bodvarsson, G. S. (1996). Hydraulic conductivity of rock fractures. *Transport in Porous Media*, *23*, 1–30. https://doi.org/10.1007/BF00145263